

## Towards an improvement of GPR-based detection of pipes and leaks in water distribution networks



A. De Coster<sup>a,\*</sup>, J.L. Pérez Medina<sup>c,e</sup>, M. Nottebaere<sup>d</sup>, K. Alkhalifeh<sup>b</sup>, X. Neyt<sup>d</sup>, J. Vanderdonck<sup>c</sup>, S. Lambot<sup>a</sup>

<sup>a</sup> Université catholique de Louvain, Earth and Life Institute, Croix du Sud 2, Box L7.05.02, 1348, Louvain-la-Neuve, Belgium

<sup>b</sup> Université catholique de Louvain, Institute of Information and Communication Technologies, Place du Levant 3, Box L5.03.02, 1348 Louvain-la-Neuve, Belgium

<sup>c</sup> Université catholique de Louvain, Louvain Research Institute in Management and Organizations, Place des doyens 1, Box L2.01.02, 1348 Louvain-la-Neuve, Belgium

<sup>d</sup> Royal Military Academy, Communication, Information, Systems and Sensors department, Avenue Renaissance 30, 1000 Brussels, Belgium

<sup>e</sup> Universidad de Las Americas, Intelligent and Interactive Systems Lab, Quito, Ecuador

### ARTICLE INFO

#### Article history:

Received 6 December 2017

Received in revised form 6 November 2018

Accepted 1 February 2019

Available online 06 February 2019

### ABSTRACT

Ground-penetrating radar (GPR) is a non-destructive tool that can be used to help detecting water leaks in water distribution networks. This study, which was undertaken in the framework of the SENSPORT project (Walloon Region, Belgium), aims at improving GPR-based detection of pipes and leaks in water distribution networks using advanced, integrated radar data processing and visualization strategies. The proposed method includes a physically-based near-field antenna effects removal approach and reflection detection and segmentation algorithms. It also involves a quantitative estimation of the medium properties using full-wave inversion. Finally, a specific human-computer interface allowing the end-user to visualize buried utilities and 2-D/3-D processed data on mobile devices is proposed. We successfully validated the general methodology through a laboratory experiment with near-field measurements performed at different times over a leaky pipe buried in a sandbox. This integrated tool appears to be promising to help detecting and monitoring water leaks. Future research will focus on more complex real cases.

Index Terms—Full-wave inversion (FWI), ground-penetrating radar (GPR), human-computer interaction, sub-surface imaging, water leaks detection.

© 2019 Elsevier B.V. All rights reserved.

### 1. Introduction

The detection of leaks in water supply systems is an essential task as the amount of water lost through leaks generally represents 20–30% of the total production. This percentage can even reach 50% for the oldest distribution networks (Charlton and Mulligan, 2001; Cheong, 1991; Colombo and Karney, 2002; Halimshah et al., 2015). These water leaks have a negative impact in terms of natural resource conservation and lead to a substantial economic loss. In addition to costs related to water production, transport and wastage, they also cause secondary financial losses through supply disruptions, erosion of pipe beds and damages engendered to buildings and road foundations. Moreover, water leaks can be at the origin of public health risks because the pressure drop occurring in defective water supply systems permits contaminant intrusions (Hunaidi et al., 2000; Rizzo, 2010). Reliable inspection techniques are therefore required to improve water leaks detection and, thereby, to optimize the management of distribution networks.

Several methods can be used to detect water leaks (Hunaidi et al., 2000; Hao et al., 2012; Liu and Kleiner, 2013; Puust et al., 2010) but the choice of the most suitable one depends on the specific case at hand. In general, the water supply companies determine the district metered area (DMA) to inspect as a priority by observing at night the water flow measured by dataloggers located at the entry and the exit of the network districts (Farley and Trow, 2003; Savić and Ferrari, 2014; Xu et al., 2014). Once a potential leak is detected, tools aiming at reducing the investigation area can be employed. Electro-acoustic devices such as leak noise correlator (Gao and Brennan, 2009; Hunaidi et al., 2004; Pal et al., 2010; Tang et al., 2009) and geophone/aquaphone (Rizzo, 2010; Fuchs and Riehle, 1991; Shimanskii et al., 2005) are commonly used to confirm and refine the presence of the leak. However, the performances of high precision acoustic devices can be affected by external acoustic interferences. Furthermore, important difficulties are encountered regarding the detection of leaks for plastic pipes, which nowadays tend to succeed metallic pipes (Hunaidi et al., 2000; Pal et al., 2010).

Thermography, which detects temperature differences between the soil and the leaking water, as well as tracer gas, which consists in dewatering and pressurizing the pipe with air and non-toxic gas, are two other high precision methods used to detect water leaks (Hunaidi

\* Corresponding author.

E-mail address: [alberic.decoester@uclouvain.be](mailto:alberic.decoester@uclouvain.be) (A. De Coster).

et al., 2000). Nevertheless, the first approach is limited by the ambient temperature and the depth of the pipe whereas the second approach is time-consuming and necessitates interrupting the water flow in the supply system. Time domain reflectometry (TDR) and electrical resistivity methods are geophysical approaches that have also demonstrated a good ability in assessing the possible presence of water leaks (Lee and Oh, 2017; Cataldo et al., 2012a; Cataldo et al., 2012b; Rucker et al., 2011). Regarding areas showing a diffused flow of water and/or having a restricted investigation volume, ground-penetrating radar (GPR) appears to be another non-destructive alternative (Ayala-Cabrera et al., 2011; Cataldo et al., 2014). It can be exploited in order to acquire high-resolution datasets and provide 3-D images of the subsurface. The discrimination of the underground structures is a substantial advantage of GPR compared to other leak detection techniques as it reduces the area to dig and limits the cost and risks associated to collateral damages (breaking other pipes, cables...).

A series of promising GPR approaches have been developed in order to help detecting and monitoring leaks in well-controlled or field conditions (Atef et al., 2016; Bertolla et al., 2014; Bimpas et al., 2010; Catapano et al., 2014; Dong et al., 2012; Glaser et al., 2012; Liu et al., 2002). The most usual one consists in identifying the water distribution pipes and comparing through visual inspection the GPR responses acquired at the initial and final stages of the leak (Ayala-Cabrera et al., 2013; Hyun et al., 2003; Nakhkash and Mahmood-Zadeh, 2004; Stampolidis et al., 2003). Several radargrams can also be collected at different times after the beginning of the leak (or water injection) to observe its temporal evolution through the subsurface radar images (Cataldo et al., 2014; Amran et al., 2017; Eyuboglu et al., 2003). For example, Demirci et al. proposed a methodology gathering a back-projection imaging algorithm with complex image subtraction and wavelet semblance analysis to detect changes in the leak region (Demirci et al., 2012). It is worth mentioning that the interpretation of the leak effects without applying an adequate image processing may be troublesome due to the geometrical spreading and the predominant surface reflection hiding the reflections backscattered by the other utilities (Cataldo et al., 2014).

Even though it provides useful information and allows studying the leak effects (Lai et al., 2016), visual inspection should be completed with

additional quantitative information. In that respect, microwave tomographic approaches have been proposed to detect pipes and bring information about their depth and their diameter (Crocco et al., 2009; Crocco et al., 2010; Hyun et al., 2007). To go further, Soldovieri et al. used the auto-focusing strategy to estimate the electromagnetic properties of the surrounding medium (Soldovieri et al., 2011). The determination of the medium electromagnetic properties provides an added value as the relative permittivity of the medium can be correlated to its water content. However, only few studies took benefit of this quantitative information to provide detailed estimates of the pipe depth and leak extent.

This paper proposes an integrated approach aiming at improving GPR-based detection of leaks. Advanced radar data processing strategies are used to maximize both the qualitative and quantitative information to be provided to end-users. Visual inspection of subsurface features is enhanced by taking advantage of a recently developed antenna effects filtering approach valid in near-field conditions (De Coster and Lambot, 2017) and a feature detection algorithm. Furthermore, accurate estimates of the pipe depth and the electromagnetic properties of the surrounding medium are also provided. These ones are obtained using a full-wave inverse modeling procedure based on the near-field antenna model developed by Lambot and André (Lambot and André, 2014; Lambot, 2014). This model does not make any simplifying assumptions related to wave propagation phenomena and takes into account antenna-medium coupling and inter-antenna interactions generally ignored in most studies. Finally, this innovative strategy proposes a visualization interface specifically designed for pipe and leak detection. The proof of concept is tested through a laboratory experiment including a leaky pipe.

## 2. Methodological aspects

### 2.1. General strategy

The innovative strategy (Fig. 1) was developed in the framework of the SENSPORT project (Wallon Region, Belgium). The radar data acquired above a suspected leak can be visualized in

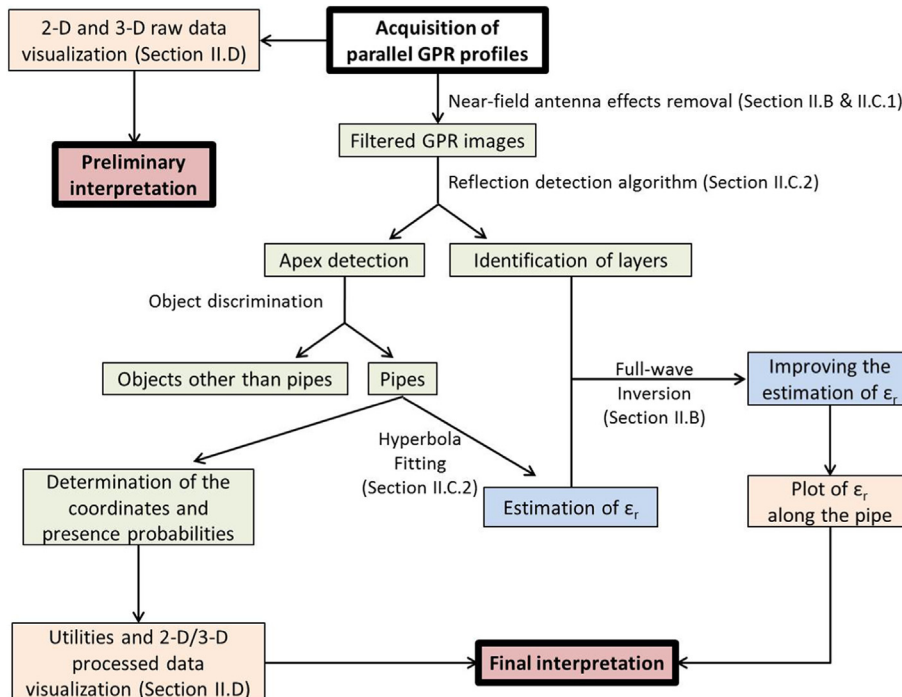


Fig. 1. General methodology helping in pipe and leak detection using GPR.

2-D and 3-D through the new visualization interface. Designed for the specific needs of the leak detection application, this visualization tool enables end-users to give a preliminary interpretation in real-time. In parallel, the acquired raw GPR data are processed based on a qualitative imaging strategy in order to facilitate the detection of buried objects. We begin by applying a physically-based approach to filter out the antenna multiple internal reflections and antenna-medium ringing from the GPR data acquired in near-field conditions. We subsequently identify the layers and buried objects (e.g., pipes, stones ...) in the filtered GPR cross-sections based on their specific signatures. The pipes are discriminated from other utilities using an algorithm that (1) detects the hyperbola apexes in the 3-D GPR dataset and (2) resorts to a specific optimization procedure to find the apexes that are likely to be related to the presence of a pipe. The coordinates of the apexes and identified pipes are subsequently sent to be visualized through the human-computer interface. A feedback on the pipe detection reliability is also provided by attributing a false alarm probability expressed through a color scale.

In order to perform the conversion between the propagation time at which the reflection of the object occurs and its actual depth, the relative permittivity of the medium ( $\epsilon_r$ ) has to be determined. The estimation of  $\epsilon_r$  represents also an important indicator regarding the leak position as it allows deriving the water content of the medium through, for instance, petrophysical relationships (Topp et al., 1980; Ledieu et al., 1986). The relative permittivity of the medium can be determined based on the linear and hyperbolic reflections generated by the contrasts existing between the electromagnetic properties characterizing two different materials. The exact shape of the hyperbola depends on the size of the object and the relative permittivity and/or conductivity contrasts existing between this one and the surrounding medium. Assuming a known object size, an estimation of the permittivity can thus be obtained by extracting the value which generates the hyperbola that best fits the measurements. This first estimate of the permittivity is then refined by resorting to the combination of the full-wave inversion (FWI) method with the near-field electromagnetic model developed by Lambot and André (Lambot and André, 2014; Lambot, 2014). The observation of the relative permittivity values along the pipe gives additional information contributing to the general interpretation of GPR data, and hence, helping in the detection of water leaks.

## 2.2. Near-field antenna model

### 2.2.1. Model formulation

The GPR full-wave model used in this paper (Lambot and André, 2014) relies on an intrinsic antenna representation and a full-wave solution of the 3-D Maxwell's equations for wave propagation in planar layered media. This model is a generalization of the far-field radar model proposed by Lambot et al. (Lambot et al., 2004) and applies to near-field conditions, which are the conditions of interest regarding pipes and leaks detection. The model takes into account the antenna radiation properties by considering an equivalent set of infinitesimal source/field points and the superposition principle. The wave propagation between the radar reference plane and these source/field points is described through complex and frequency-dependent global reflection and transmission coefficients, accounting for the variations of impedance within the antenna and describing the antenna-medium coupling. The generalized radar equation is formulated in the frequency domain as follows (Lambot and André, 2014):

$$S(\omega) = \frac{b(\omega)}{a(\omega)} = T_0(\omega) + \mathbf{T}_s (\mathbf{I}_N - \mathbf{G}^0 \mathbf{R}_s)^{-1} \mathbf{G} \mathbf{T}_i \quad (1)$$

where  $S(\omega)$  denotes the radar signal, i.e., the ratio between the backscattered field  $b(\omega)$  and the incident field  $a(\omega)$  at the radar reference plane,  $\omega$  refers to the angular frequency,  $\mathbf{I}_N$  is the  $N$ -order identity matrix where  $N$  is the number of point sources or field points,  $T_0(\omega)$  is the global transmission/global reflection coefficient of the antenna in free space,  $T_i(\omega)$  denotes the global transmission coefficient for the field incident from the radar reference plane onto the source points,  $T_s(\omega)$  is the global transmission coefficient for the fields from the source points onto the radar reference plane and  $R_s(\omega)$  is the global reflection coefficient for fields incident from the layered medium onto the field points and, in particular, permits to account for the multiple wave reflections between the antenna and the medium (antenna-medium coupling). These antenna characteristic coefficients are needed to filter out antenna effects from the raw radar data and to estimate the medium electromagnetic properties. They are determined through the specific calibration procedure detailed in Lambot and André (2014).  $G(\omega)$  and  $G^0(\omega)$  denote the layered medium Green's functions, i.e., the exact solutions of the 3-D Maxwell's equations describing wave propagation in multilayered media and refer, respectively, to the transmitter-receiver and receiver-receiver Green's functions.

### 2.2.2. Full-wave inverse modeling approach

The strategy adopted to retrieve the medium properties consists in inverting the near-field GPR data, which results in a non-linear optimization problem. To tackle this issue, we combine the model previously formulated with a full-wave inversion procedure. The inversion problem is formulated in the least-squares sense and the objective function  $\phi(\mathbf{b})$  to be minimized is formulated as follows:

$$\phi(\mathbf{b}) = \|\mathbf{S}^* - \mathbf{S}\|^T \|\mathbf{S}^* - \mathbf{S}\| \quad (2)$$

where  $\mathbf{S}^* = S(\omega)$  and  $\mathbf{S} = S(\omega, \mathbf{b})$  are the vectors containing, respectively, the observed and the simulated radar data,  $T$  denotes transpose and  $\mathbf{b}$  is the parameter vector  $[\epsilon_r, \sigma_k, h_k]$  containing the relative permittivity  $\epsilon_r$ , the electric conductivity  $\sigma$  and the layer thickness  $h$  values, with  $k = 1, \dots, K$  representing the layer index. In order to avoid the local minima found in multi-dimensional objective function topographies, we need to adopt an effective optimization strategy. Various signal inversion strategies have been explored with the generalized model but one of the most efficient consists in sequentially combining the Global Multilevel Coordinate Search (GMCS) (Huyer and Neumaier, 1999) with the Nelder-Mead Simplex algorithm (NMS) (Lagarias et al., 1998). The approximate relative permittivity estimation ensued from geometrical optic considerations allows reducing the parameter spaces to investigate in the full-wave optimization procedure.

## 2.3. Processing strategies

### 2.3.1. Near-field antenna effects removal

In contrast to far-field conditions, near-field conditions do not permit to analytically filter out antenna effects from GPR data (Lambot et al., 2004). In that respect, De Coster and Lambot (De Coster and Lambot, 2017) proposed a full-wave, numerical antenna effects filtering method that allows filtering out the antenna multiple internal reflections, the antenna-medium ringing and the antenna height effects from GPR data acquired in near-field conditions above a locally multilayered medium. The main idea of the removal approach is that any multilayered medium can be reduced to a half-space medium characterized by a frequency-dependent global reflection coefficient, and hence, by an effective permittivity ( $\epsilon_{eff}(\omega)$ ) and an effective conductivity ( $\sigma_{eff}(\omega)$ ). This substitution represents an exact mathematical equivalence as these properties account for all reflections in the original layered medium. The antenna effects removal strategy assumes that the antenna height can be determined independently.

The optimization scheme described in Section 2.2.2 is used to retrieve these effective parameters independently for each frequency-position couple. Based on these properties, we are able to compute the so-called complex effective conductivity ( $\eta_{eff}(\omega)$ ) found in the frequency domain Maxwell's equations as follows:

$$\eta_{eff}(\omega) = \sigma_{eff}(\omega) + j\omega\epsilon_{eff}(\omega) \quad (3)$$

The conversion of  $\eta_{eff}(\omega)$  into the time domain ( $\eta_{eff}(t)$ ) is subsequently performed using the Inverse Fourier Transform:

$$\eta_{eff}(t) = \frac{1}{2\pi} \int_{-\infty}^{\infty} \eta_{eff}(\omega) e^{j\omega t} d\omega \quad (4)$$

The obtained quantity represents a filtered radar image for which time zero exactly corresponds to the first medium interface. Please refer to (De Coster and Lambot, 2017) to get more details about this antenna effects filtering procedure.

### 2.3.2. Utilities detection and structural imagery

This section describes the multi-stage detection methodology used to (1) detect the buried pipes in the filtered GPR cross-sections and (2) provide an estimation of the surrounding permittivity. The first step consists in applying the so-called 'range-compression' operation on 1-D GPR signals (Skolnik, 2008) and subsequently selecting the echoes having an amplitude exceeding a detection threshold. The second step involves the detection of the layer interfaces within the investigated medium. To achieve this task, a depth histogram is generated based on the range-compressed data. The sharp peaks identified in the histogram therefore shows up the horizontal layers that are detectable. It is worth noting that the method could be generalized to non-horizontal planes and planes that are not observed along the entire profile.

In a third step, the procedure aiming at detecting the underground scattering objects is carried out. These objects are generally characterized by hyperbolic-shaped signatures in GPR cross-sections. The method consists in finding the connected components within a cross-section and identifying the hyperbola apex candidates. More details regarding this methodological aspects are available in Ardekani et al. (2014). Based on the position of the antenna and the localization of the hyperbola apex, it is possible to estimate the local relative permittivity of the medium above the object using a hyperbola fitting procedure. Synthetic hyperbolas are generated by implementing different values of  $\epsilon_r$  in a hyperbola model. The  $\epsilon_r$  value minimizing the error between the modeled and detected hyperbolas is then selected.

The configuration generally considered to relate the hyperbola characteristics to GPR data is shown in Fig. 2. For a given antenna position  $x$ , the time at which the object reflection is recorded  $t_r$  depends on two factors: the distance separating the antenna from the object  $d$  and the velocity of the wave traveling through the

medium  $v$ . Considering the scenario shown in Fig. 2 and a monostatic configuration (zero-offset transmitter-receiver), the antenna-object distance can be calculated with the Pythagorean theorem as follow:

$$d = \sqrt{z_0^2 + (x-x_0)^2} \quad (5)$$

where  $z_0$  is the object depth and  $(x - x_0)$  is the distance between the antenna position  $x$  and the center of the hyperbola  $x_0$ . Assuming geometric optic approximations and a non point-like object (i.e., characterized by a radius  $r$ ), the reflection detection time is defined as follows:

$$t_r = \frac{2(d-r)\sqrt{\epsilon_r}}{c} \quad (6)$$

where  $c$  is the speed of light in free space. In this relation, the permittivity of the medium above the object and the diameter of the object are the unknowns that have to be estimated. The rest of the parameters can be derived from the information provided by the GPR image. Note that this approach considers a negligible soil conductivity and the medium as being homogeneous.

For longitudinal objects such as pipes or cables, the 2-D model described does not hold anymore because the orientation of the object is not necessarily perpendicular to the cross-section. Therefore, we introduce another relationship that takes into account the 3-D orientation of a cylindrical pipe having a radius  $r$ :

$$t_r = \frac{2(d_{3D}(p_0, p_1) - r)}{v} \quad (7)$$

where  $d_{3D}(p_0, p_1)$  is the distance between the position of the antenna  $(x, y, 0)$  and the axis of the pipe going from the start point  $p_0 = (x_0, y_0, z_0)$  to the endpoint  $p_1 = (x_1, y_1, z_1)$ . The number of layers detected between the soil surface and a given object is another important factor as the relative permittivity contrasts influence wave propagation and, hence, the shape of the hyperbola. Therefore, if the number of layers above the scattering object  $n$  is superior to one, we derive what we call an equivalent relative permittivity  $\epsilon_{re}$ . It actually represents a combination of the permittivities characterizing the layers located above the object:

$$\epsilon_{re} = \frac{ct_{0n}}{\sum_{i=1}^{n-1} \left( \frac{d_i}{\sqrt{\epsilon_{r,i}}} + \frac{z_n}{\sqrt{\epsilon_{r,i}}} \right)} \quad (8)$$

where  $z_n$  is the distance between the object and the interface of the layer  $n$ . By resorting to Eq. (8) and proceeding recursively from the top layer to the bottom layer, the relative permittivity of each layer can be obtained, as detailed in Ardekani et al. (2014). This approach requires the presence of at least one object within each layer. It is worth noting that this proposed method based on straight-ray propagation remains approximate.

### 2.4. End-user interface and visualization software

Instead of relying on a multi-purpose simulation or visualization software, a software has been developed to import, to visualize, and to exploit 3-D GPR data specifically for the SENSPOINT project. Some requirements were elicited from water technicians, who are not necessarily GPR experts. The import, the visualization, and the exploitation of raw data should be as straightforward as possible to streamline the process. Consequently, no prior modeling, simulation, or parameterization of a scene is imposed. The visualization should focus on the filters that render ground objects, such as pipes and water leaks, as quick and usable as possible, while enabling some flexibility. Consequently, the software should focus on filtering techniques that are targeted

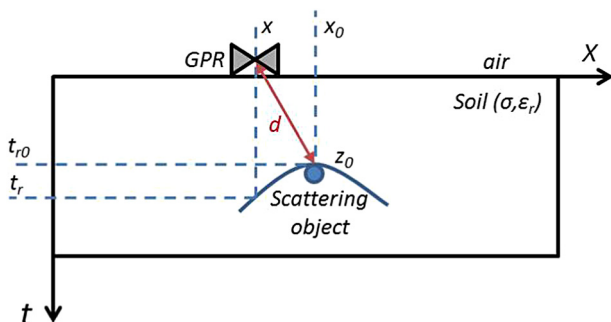
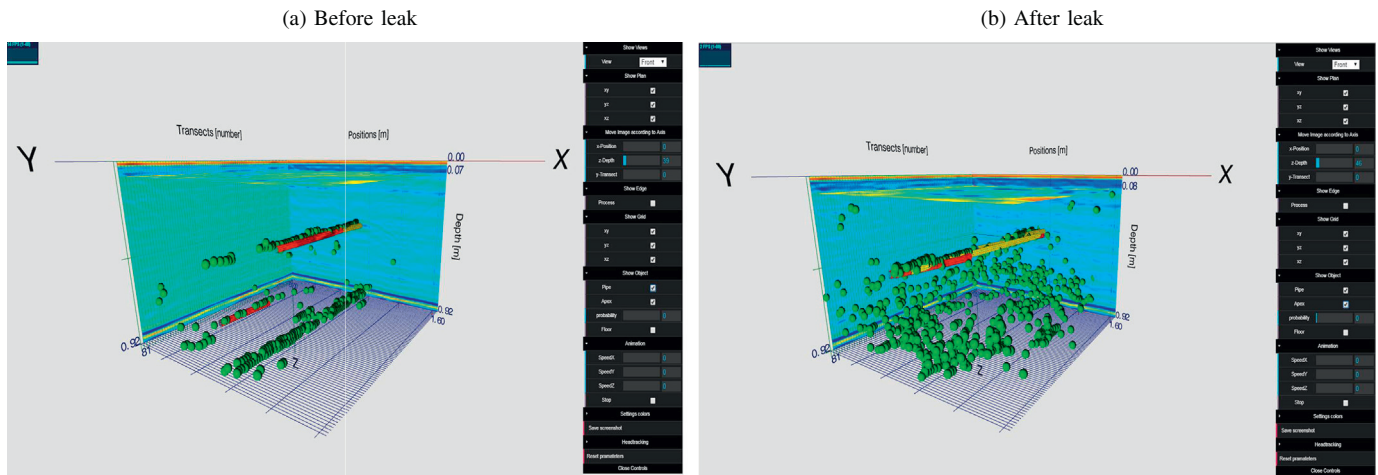


Fig. 2. Reflection hyperbola caused by a point scatterer.



**Fig. 3.** Interface developed for 3-D GPR data visualization and representation of the pipes and the apices in the scene. Visualization at (a) the initial stage ( $t_0$ ) and (b) final stage ( $t_{end}$ ) of the leak.

to the project goal. This section discusses the different scientific and implementation choices made for fulfilling these requirements, in order to maximize the usability of the resulting software.

#### 2.4.1. Development of the visualization tool

A Collaborative User Centered Design (CUCD) method (Medina and Vanderdonck, 2016) has been applied with three stages that are subsequently presented: (1) elicitation of end users' requirements and modeling the context of use, (2) development of a visualization technique appropriate for 2/3-D GPR raw data, and (3) iterative prototyping of a multi-device, multi-platform user interface.

The context of use is defined as a triple  $C = (U, P, E)$  (Calvary et al., 2003), where  $U$  denotes a user model describing the user profile (e.g., cognitive style, preferences) and related tasks,  $P$  denotes a platform model (e.g., minimal screen size and resolution), and  $E$  denotes an environment model (e.g., outdoor parameters). In particular, a task model was captured from end user to express their tasks independently of any technology. A task model recursively decomposes a task into sub-tasks to end up with actions and initiate a model-based approach for designing a usable interface (Vanderdonck, 2005). From the task model, an Abstract User Interface is derived and materialized into a series of specifications to feed the user interface prototyping.

To fulfil the requirements in the third stage, a web-browser solution should be developed that is accessible through the Internet with zero-install (i.e., no setup, no install, no plug-in, no add-on), working on any device (e.g., ranging from a tablet to a large monitor) and on any operating system (e.g., no particular systems is imposed). We performed an analytical comparison of existing visualization frameworks<sup>1</sup> based on the following criteria: compatibility with Web technology, support of multi-device and multi-platform capabilities, performance of data visualization, and open access.

HighchartsJS and D3 libraries directly display raw data as a set of points located in a 3-D space with their  $x$ ,  $y$  and  $z$  coordinates and a color coding scheme depending on the radar data amplitude. As a result, the processing time significantly increases with the number of considered points, which is incompatible with GPR surveys where more than 1 million points are typically required to investigate a 9 m<sup>2</sup> surface area. HighchartJS does not support datasets with more than 999 points. Therefore, Three.js library was selected to display GPR data as

manipulable images in Portable Network Graphics (PNG) format instead of point clouds.

#### 2.4.2. GPR data visualization interface

Beyond the processing of very large datasets, their visualization on small screens remains challenging for satisfying the multi-device requirement, especially when a low-end device suffers from limited screen size, resolution, and computational power. In address this challenge, the 2-D Starfield display visualization technique (Ahlberg and Shneiderman, 1994) is generalized into a 3-D galaxy-based visualization technique for small screens, based on the combination of three principles: tight coupling of dynamic query filters with starfield displays. In this visualization technique, images are subject to direct manipulation through query parameters that are rapidly adjusted with sliders, buttons, which immediately result into the update of their visualization in real time. Queries are processed dynamically on the data set instead on a physical database to provide immediate feedback. Coupling a dataset with access features enables the end user to effectively and efficiently explore large amounts of data (Burigat and Chittaro, 2009): direct manipulation features, such as zoom in/out, 3-D plane perspectives, optimize the limited space available on small screens. This visualization technique benefits from a reasonable task completion time and an acceptable satisfaction rate among users who, when interacting with a small screen, prefer to keep a complete contextual overview while manipulating the data, as opposed to a simple zooming interface (Buering et al., 2006).

The visualization interface is composed of three main elements (Fig. 3): (1) a scene containing the radar images represented in 3-D ( $X, Y, Z$ ), (2) a menu containing the visualization features (in Appendix) based on the aforementioned principles, and (3) the image of the area where the radar data were acquired, which identifies the location where the study was conducted to be later integrated into a geographic information system.

#### 2.4.3. Image filter analyses

To support the interpretation of the raw data, 21 image filtering techniques were compared to reach a balance between capability of extracting relevant information (e.g., pipes and leaks) with enough contrast, reduction of background noise, and overall execution time. The filter requiring a lower processing time is the threshold usually employed. Nevertheless, it does not give a good overview of the contrast present in the remaining part of the data. Based on this comparison, images are filtered with the Sobel operator (Kanopoulos et al., 1988; Vincent and Folorunso, 2009) or the Frei-Chen edge detector algorithm (Park, 1990). Despite their high execution time, these ones give an

<sup>1</sup> D3, <http://d3js.org/>; HighchartsJS, <http://www.highcharts.com/>, ThreeJS <http://threejs.org/>

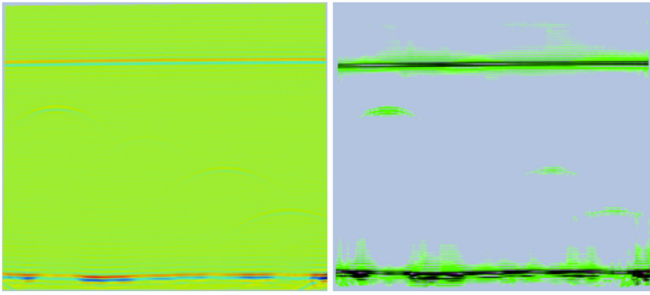


Fig. 4. Image before and after applying the Frei-Chen edge detector algorithm and a threshold value.

efficient detection of edges and contrasts in images. The Frei-Chen edge detector shows performance characteristics similar to the Sobel operator, but with a slightly better edge detection (Fig. 4). The Frei-Chen edge detector is revealed more efficient because it includes a normalization factor as well as other factors that are meant to exclude all features that are not edges. This detector works better because it is less sensitive to noisy data than the Sobel operator and is more efficient to detect edges created by small gradient. Both image filtering techniques were implemented in the visualization application.

The user interface integrates in the 3-D visualization space the pipes and apexes recognized during the utility detection stage. The final user can filter the number of pipes and apexes depending on the index density value attributed to each point. This parameter can be easily visualized as its magnitude is expressed according to a color scale. A rough estimation of the relative permittivity of the medium surrounding the pipes and an apex density index, which can be seen as a probability value. It provides a feedback on the reliability related to pipes detection.

### 3. Description of the laboratory experiment

A laboratory experiment was conducted in the Georadar Research Center of the Université catholique de Louvain (<http://sites.uclouvain.be/gprlouvain>) in order to assess the proposed integrated methodology. To achieve this goal, we used a stepped-frequency continuous-wave radar system composed of a vector network analyzer (VNA, ZNB8, Rhode & Schwarz, Munich, Germany) and a homemade Vivaldi antenna (Sarkis and Craeye, 2010) operating between 800 MHz–3500 MHz (Fig. 5). The 3-D Vivaldi antenna has been designed and meshed using the GMSH (Geuzaine and Remacle, 2009) freely available software. A software developed at UCL based on the Method of Moments is used to simulate the structure (Dardenne and Craeye, 2008; Alkhalifeh et al., 2014; Alkhalifeh et al., 2016). 3-D metallic antenna structures are mainly proposed to reduce the loss in the dielectric part of the feed. A direct coax

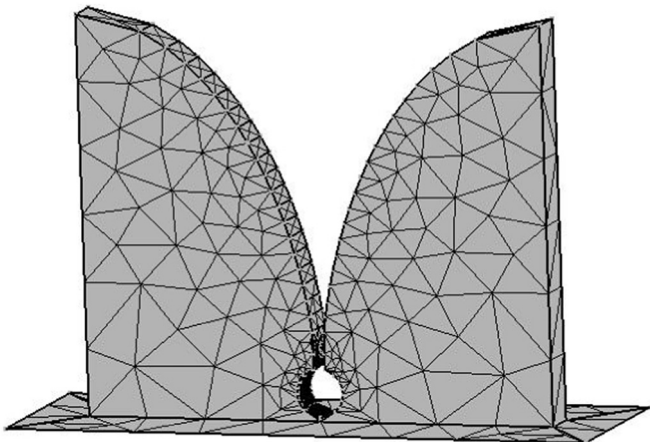


Fig. 5. Mesh of the Vivaldi antenna used in the experiment.

feeding technique is used which avoids the need for balun matching circuits. Another advantage of using this technique is that no soldering for the feed is needed. Such a robust feeding technique is important for antennas which are exposed to often repeated measurements. The 3-D Vivaldi antenna can be made hollow, so as to house the low-noise amplifier, which is then shielded from external fields and close enough to the antenna feeding point (Sarkis et al., 2011).

We used a frequency step of 50 MHz, thereby resulting in 55 frequencies. The antenna acted as a transmitter-receiver unit (monostatic mode) and was connected by a 50- $\Omega$  impedance coaxial cable to the reflection port of the VNA. The latter was calibrated at the connection between the antenna feed point and the coaxial cable using a standard Open-Short-Match calibration kit. The antenna, which presents an aperture of 24 cm and a height of 15 cm, was calibrated for near-field conditions. About 100 GPR measurements were carried out at distances ranging from 0 m to 0.70 m over a  $3 \times 3$  m<sup>2</sup> copper plate acting as a perfect electrical conductor (PEC). The antenna was modeled using 8 source/field points distributed over the antenna aperture. A two-stage optimization approach was used to determine the antenna transfer functions as the near-field calibration procedure is a non-linear inverse problem. First, following the approach presented in Lambot et al. (2006), the measurements acquired in far-field (i.e., above  $1.2 \times$  the size of the antenna aperture) were used to estimate the far-field transfer functions. Then, these coefficient were updated for near-field conditions by (1) adding a subset of near-field radar measurements acquired at the highest distances to the initial subset, (2) running a local optimization algorithm with initial guesses as the starting point and (3) iterating steps (1) and (2) until the full dataset is used. More detailed information is available in Lambot and André (2014) (Lambot and André, 2014).

Measurements were performed with the Vivaldi antenna at 5 cm above a  $3 \times 3 \times 1$  m<sup>3</sup> sandbox in which a plastic pipe was buried (Fig. 6). A copper sheet working as a PEC was placed at the bottom of the sand layer to avoid unidentified reflections from the underlying materials. The 2 m long pipe had an outer diameter of 32 mm and was located at about 0.389 m depth. Compared to the water supply pipe configurations generally encountered in urban areas, the diameter and burial depth of the pipe were scaled down by a factor 1/3. The two extremities of the pipe were beforehand connected to one meter long pipes to facilitate the continuous filling of the pipe with water and avoid the appearance of air bubbles during the leak experiment. A hole having a diameter of 1 mm was previously drilled at the top of the pipe and a nylon membrane (aperture 50  $\mu$ m) was stuck on it before filling the buried pipe with water. The nylon membrane allowed simulating a leak while avoiding sand intrusion in the pipe.

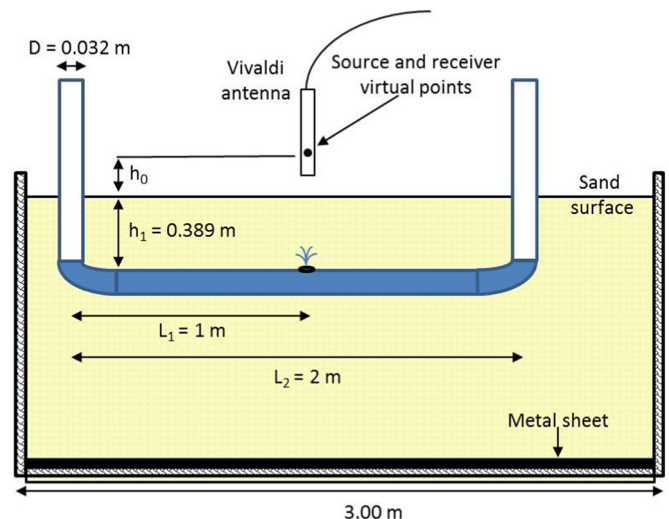


Fig. 6. Laboratory scaled-down setup used for water leak detection.

**Table 1**  
Scanning times  $t_i$  and volumes of water added after each transect acquisition ( $V_{add}$ ).

Scan	Scanning times [min]	$V_{add}$ [ml]
$t_0$	0	1500
$t_1$	35	450
$t_2$	75	200
$t_3$	113	150
$t_4$	152	120
$t_5$	190	60
$t_6$	284	80
$t_7$	385	85
$t_8$	1385	/

Then, we added enough water to fill the pipe but without generating a leak and performed a first set of measurements at a scanning time called  $t_0$ . We acquired 81 profiles perpendicular to the pipe in order to provide a 3-D image of the subsurface. The profiles were spaced by 0.02 m and had a length of 1.60 m. We mounted the radar on an automated XYZ positioning system and used a computer to remotely control the acquisition process, i.e., to automatically move the radar to the required positions and to carry out the measurements. Afterwards, we started pouring water into the supply pipe and acquired successive profiles at different times above the leak position. The objective of this step was twofold: (1) to investigate in the collected radar images the visual changes occurring in presence of a small leak and (2) to quantitatively assess the evolution of the relative permittivity of the medium, and hence, its water content, over time. To fulfil the second objective, we applied the inversion scheme described in Section 2.2.2 on the time-lapse signals acquired above the leak position. The scanning times and the volumes of water added just after each acquisition are given in Table 1. It is worth noticing that, for an equivalent duration, the volume of water added to keep a reasonable level of water into the pipe decreased. Two hypotheses are put forth to explain this phenomenon: (1) the low hydraulic conductivity value of dry sand and (2) a partial clogging of the nylon membrane. In order to simulate a more significant leak, we pressurized the pipe by sealing one of its extremities and connecting the other to a garden hose having an inner diameter of 12 mm. We let the water flowing out of the pipe during 10 min and finally acquired at the final stage of the experiment ( $t_{end}$ ) a second 3-D dataset.

The processing strategies developed in Section 2.3 were applied to each transect of the 3-D datasets acquired at the beginning and the end of the leak detection experiment. The first step consisted in removing the near-field antenna effects using the method described in De Coster et al. (2017) (De Coster and Lambot, 2017). The antenna height ( $h_0$ ) is a prerequisite of the filtering approach. Therefore, we computed it along with the sand surface relative permittivity ( $\epsilon_{r1}$ ) using the model described in Section 2.2 and full-wave inversion. We restricted the inverse problem to the surface reflection and inverted GPR data using a lookup table (LUT) method. A LUT is a matrix of signals precomputed for different combinations of parameters which enables to avoid performing time-consuming optimizations when the number of parameters and the parameter values to test are relatively small. We simulated

the signals for all combinations of values belonging to the following ranges:  $h_0 = [0.04: 0.001: 0.06]$  m and  $\epsilon_{r1} = [2.0: 0.1: 3.5]$ . The sand electrical conductivity was neglected (0 S/m) as the influence of this parameter on the signal is negligible in that frequency range. The boundaries of  $\epsilon_{r1}$  were set in accordance with the laboratory measurements previously performed on the dry sand. We assumed that the leak does not affect the surface reflection. The detection of the reflection hyperbolas and layers was subsequently applied to the filtered images. After identifying the location of the potential pipes, their coordinates in the 3-D space were determined and sent to the visualization interface described in Section 2.4.

The hyperbola fitting procedure described in Section 2.3.2 was applied to give a first estimation of the subsurface relative permittivity along the pipe. The inversion strategy developed in Section 2.2.2 was subsequently used to refine the electromagnetic properties of the medium above the pipe. Inversions were carried out using 55 frequencies by considering the parameter space boundaries defined as follows:  $2 < \epsilon_{r,2} < 10$  and  $0.35 \text{ m} < h_1 < 0.45 \text{ m}$ . The antenna height and the surface relative permittivity computed in the previous step were implemented as known parameters in the inversions. The electrical conductivities were assumed to be negligible. The upper boundary of  $\epsilon_{r,2}$  was limited to 10 based on results provided through the hyperbola fitting procedure. The boundaries of the second parameter were set following two considerations. Firstly, the upper boundary corresponds to the maximal depth at which operators bury pipes scaled down by the factor 1/3. Secondly, the parametric space should be centred on pipe depth estimated based on the filtered radargram and straight ray approximation. The parametric spaces used in inversions were kept identical during the whole leak experiment and about 1200 iterations were run for each signal. Nevertheless, we permitted the local algorithm to overcome the boundaries if the response surface topography leads to a global minimum located at the limit of the parametric space. The relative permittivity values retrieved along the pipe were then plotted for each 3-D dataset (initial and final leak stages) in order to be compared.

## 4. Results and 3-D visualization

### 4.1. Antenna calibration

The antenna heights implemented in the calibration procedure were limited to those varying from 0.028 m to 0.427 m to minimize errors in the retrieved antenna transfer functions. The global reflection and transmission coefficients were used to model signals corresponding to those measured during the calibration procedure. Fig. 7 shows the measured and modeled radar data as well as the difference between both in the time domain. We can identify in Fig. 7a and Fig. 7b the internal antenna reflections as well as the PEC reflection and the multiple reflections associated to this one. A good match is observed between the modeled and measured signals since the relative error in terms of signal amplitude remains below 2%. The calculated correlation coefficient is equal to 0.9999, thereby demonstrating that a good calibration was achieved.

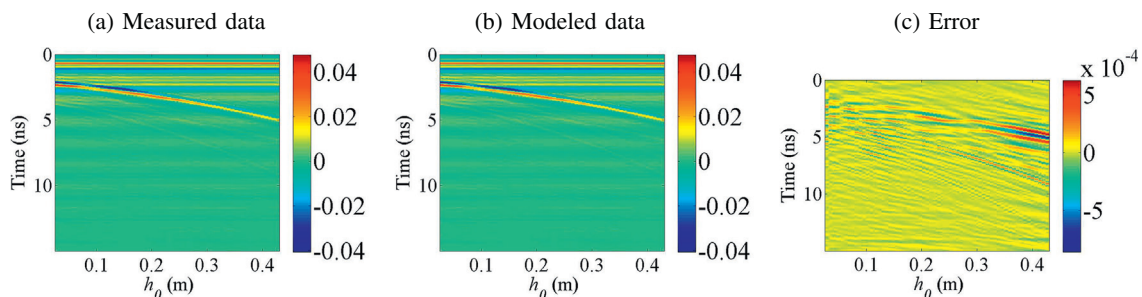


**Fig. 7.** (a) Measured and (b) modeled radar data related to the calibration setup. The error (c) represents the difference between both signals.

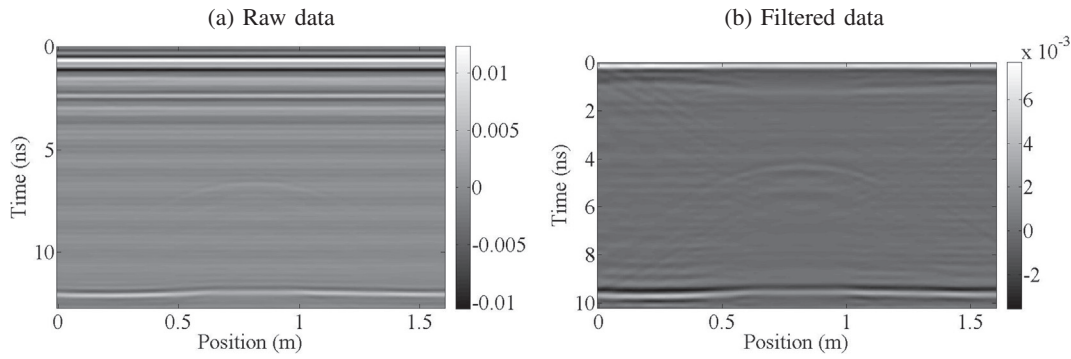


Fig. 8. Image of the (a) raw and (b) numerically filtered radar data for measurements performed at about 5 cm above the sand surface.

#### 4.2. Qualitative analysis of the leak effects

The image of the raw GPR data acquired at about 5 cm above the sandbox at the scanning time  $t_0$ , i.e., with no leak but with the pipe filled with water, is shown in Fig. 8a. The pipe buried into the sand and the PEC placed at the bottom of the sandbox are visible at about 6.5 ns and 12.0 ns, respectively. Difficulties are encountered to detect the sand surface because the surface reflection is mixed with the antenna multiple internal reflections. As mentioned earlier, the antenna effects filtering approach requires the determination of the antenna height in every position. The antenna height estimated using full-wave inversion oscillates between 0.045 m and 0.052 m with a mean value equal to 0.0485 m whereas the surface relative permittivity ranges between 2.51 and 2.72 with a mean value equal to 2.63. The relative permittivity values calculated through inversions are therefore in agreement with those expected for dry sand.

The image obtained after applying the proposed antenna filtering method and a convolution with a Mexican hat wavelet is shown in Fig. 8b. The convolution step was performed to minimize the spectral leakage effects partly generated by the Inverse Fourier Transform. The radargram evidences that the antenna internal reflections and the antenna-medium multiple reflections have been successfully removed. As a result, the PEC and the pipe are clearly identified in the filtered image despite the presence of some sandbox edge effects characterized by the diagonal lines starting from the corners. We also observe a well defined surface reflection located at 0 ns. It is explained by the fact that the reflection coefficient is computed at the surface of the medium. This reflection is constant because the antenna height variation effect is removed by the numerical filtering procedure. Based on the filtered data and the mean relative permittivity value determined through inversions, we were able to estimate the depth of the pipe. We calculated a pipe depth of 39.2 cm using the straight ray approximation, which corresponds approximately to the value expected from the laboratory measurements (0.389 m).

After triggering the low-pressure leak, i.e., after having added water in the pipe to provoke a hydraulic load, we acquired several transects above the leak position to monitor its development. The filtered images of the data acquired 35 min and 284 min after the start of the leak are shown in Fig. 9a and b, respectively. Some discrepancies due to changes of the water content with time are observed, especially around and below the location of the leak. First, the water flowing out of the pipe increases the water content of the sand surrounding the pipe, which causes a distortion of the backscattered signals, and hence, a degradation of the hyperbolic shape of the reflection. Secondly, after some time, the continuity of the PEC reflection is interrupted at the position located beneath the leak. This phenomenon is caused by the augmentation of the relative permittivity of the sand which in turn leads to a decrease of the wave velocity. Finally, the PEC reflection amplitude beneath the leak position decreases because of the attenuation of the

electromagnetic waves traveling through the wetter area. The observed effects gain in importance as time goes on. Fig. 9c shows the transect acquired after simulating the pressurized leak. As expected, the larger volume of water that flowed out of the pipe influenced the part of the signal arriving before the pipe reflection and enhanced the leak effects previously cited. The PEC reflection is affected over a wider

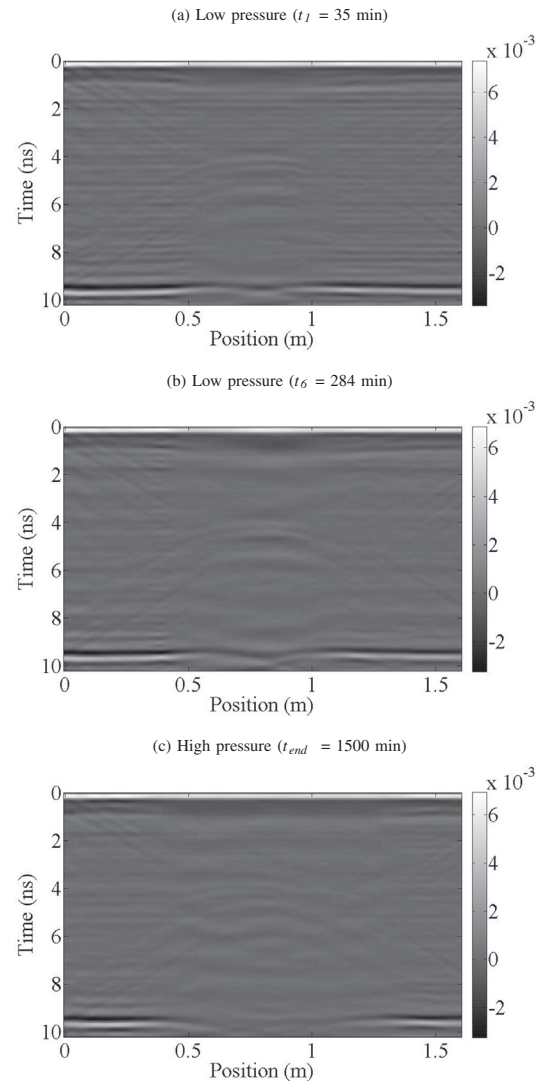


Fig. 9. Images of the filtered radar data for measurements performed above the low-pressure leak after (a) 35 min and (b) 284 min as well as above (c) the high-pressure leak.

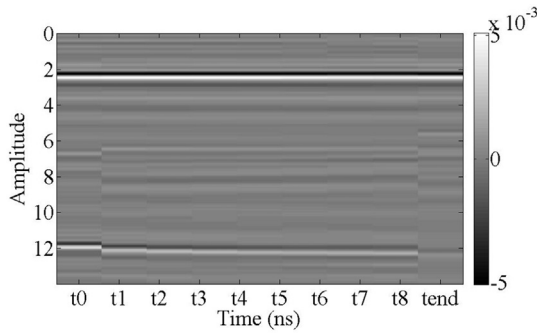


Fig. 10. Signals acquired above the leak at the different moments specified in Table 1.

distance and the hyperbolic reflection accounting for the pipe is not clearly visible.

In order to have an overview of the leak effects, we gathered and compared in Fig. 10 the spatially-coincident signals acquired at the different stages of the leak (scanning times are described in Table 1). After 35 min of leak, two main differences can be distinguished compared to the initial situation: (1) some substantial disturbances affect the signal under the pipe and (2) the second more important reflection, that is assumed to be attributed to the pipe, arrives slightly before a propagation time equal to 6.45 ns ( $t_1$  to  $t_8$ ) instead of 6.70 ns ( $t_0$ ). The first difference is caused by the water flowing through the medium towards the bottom of the sandbox. The water is in this case mainly drained by gravity and is accumulated at the level of the PEC. The earlier arriving time of the reflection recorded by the radar is explained by the dampening of the sand located just above the leak. The capillarity rise is restricted to a few centimeters because of the coarse texture of the sand and the small hydraulic conductivity value characterizing the dry sand. This capillarity front accounts for the reflection observed at 6.45 ns and explains why the perturbation arrives earlier in the recorded signal. Two other effects due to the increase of the medium permittivity below the pipe can be observed at the level of the PEC reflection (Fig. 10): (1) a reduction of the reflection amplitude and (2) a delay in the reflection time. The importance of the mentioned effects is increased with the pressurized leak (see  $t_{end}$ ).

#### 4.3. Quantitative analysis of the leak effects

We conducted an inversion on the signal located just above the leak for each successive transect acquired with the GPR system. Fig. 11 shows the fit between the measured and the modeled data before the leak was initiated. The reflection accounting for

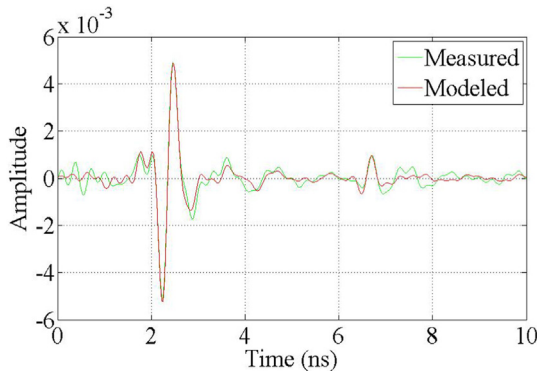


Fig. 11. Measured signal and modeled signal in the time domain before the beginning of the leak ( $t_0$ ).

**Table 2**  
Values of the parameters retrieved by inverting the signals acquired at different moments above the leak.

Scanning time	$h_0$ [m]	$\epsilon_{r1}$ [-]	$h_1$ [m]	$\epsilon_{r2}$ [-]
$t_0$	0.048	2.73	0.385	3.95
$t_1$	0.048	2.74	0.362	3.43
$t_2$	0.048	2.74	0.361	3.38
$t_3$	0.048	2.73	0.362	3.34
$t_4$	0.048	2.72	0.363	3.27
$t_5$	0.048	2.67	0.365	3.22
$t_6$	0.047	2.56	0.373	3.00
$t_7$	0.047	2.52	0.375	2.88
$t_8$	0.048	2.66	0.384	2.40
$t_{end}$	0.048	2.64	0.293	3.32

the air-sand interface and for the pipe are detected at 2.35 ns and 6.70 ns, respectively. We observe that both reflections are adequately modeled. Nevertheless, signal perturbations are observed below the pipe reflection. These perturbations are not well reproduced as it is difficult to take these heterogeneities into account in the multilayered modeling approach. The value retrieved for the different parameters are summarized in Table 2. The parameter estimates retrieved regarding the antenna height, the relative permittivity of the sand and the depth of the pipe seem to be consistent with the values expected for the dry sand.

The fit between the modeled data and the data measured 35 min after the beginning of the leak (Fig. 12) evidences that the model reproduces well the measurements and confirms the assumptions previously formulated. In terms of parameters (see Table 2), the leak is translated by (1) the decrease of the pipe depth ( $h_1$ ) and (2) the decrease of the relative permittivity of the second layer. This second observation is caused by the quite weak contrast existing between the dry sand and the slightly wet sand. The measurements show that, even if the sand thickness affected by the leak is increased, the wetting front remained at the same position between  $t_1$  and  $t_5$ . The values of the parameters estimated through inversions are pretty much the same because, in the case of a low-pressure leak, the water slowly spreads all over the sand and does not cause significant change of the signal above the leak position.

At  $t_6$ ,  $t_7$  and  $t_8$ , we observed a decrease of the second layer permittivity and an increase of the layer depth. However, as shown in Fig. 10, no substantial reflection shift occurred at the level of the wetting front reflection. This is likely to originate from the difference between the model used for the inversions (layered medium) and the reality at some stage of the infiltration (continuous changes in permittivity). The water that leaked from the pipe substantially distorted the signal

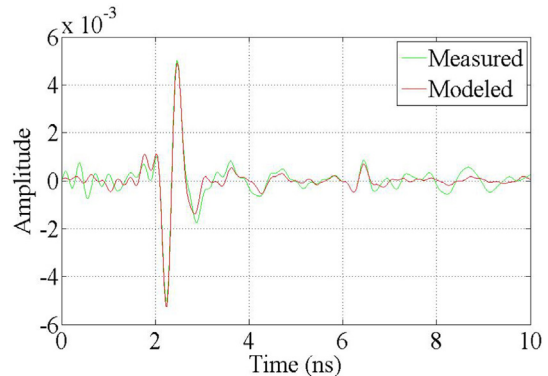
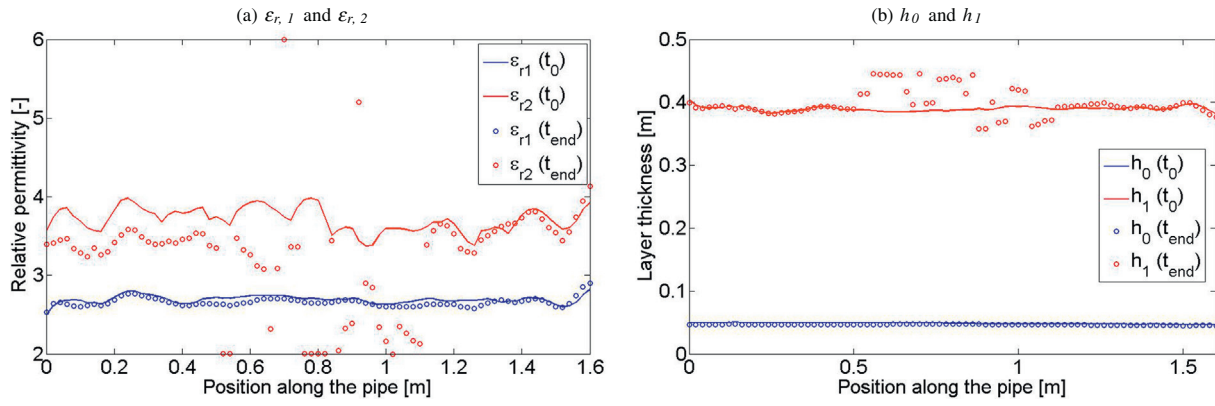


Fig. 12. Measured signal and modeled signal in the time domain 35 min after the beginning of the leak ( $t_1$ ).



**Fig. 13.** Values of the parameters computed along the pipe before ( $t_0$ ) and at the end ( $t_{end}$ ) of the leak with (a) the relative permittivity of the sand ( $\epsilon_{r,1}$ ) and the water pipe ( $\epsilon_{r,2}$ ) layers and (b) the antenna height ( $h_0$ ) and pipe depth ( $h_1$ ).

under the leak position, which engendered a reflection having a relatively high amplitude. Without a priori knowledge, the appearance of this second important reflection prevents the automatic detection of the sand-pipe contrast and leads sometimes the optimization algorithms towards a wrong solution. Analyses of the objective function topography (not shown here) for different configurations also indicated possible issues related to non-uniqueness of the solution at some stage of the infiltration. The algorithms used to invert the data seemed to be trapped in a local minimum because of the correlation existing between  $h_1$  and  $\epsilon_{r,2}$ . In this case, the decrease of  $\epsilon_{r,2}$  (increase of the wave velocity) is compensated by the retrieval of a thicker  $h_1$ , which therefore gives a reflection arriving at the same propagation time. The inversion conducted on the signal acquired at the end of the leak experiment ( $t_{end}$ ) was successful and evidences that putting water under pressure caused a larger rise of the capillary fringe.

The knowledge of the electromagnetic properties of the materials surrounding the pipe is important as these ones control wave propagation. This quantitative information can be used to determine where are situated the wetter areas and estimate the depth at which the objects are buried. In the case of a water leak, we assume a variation of these properties along the pipe. Therefore, in order to validate this assumption, inversions were performed on data acquired before generating the leak ( $t_0$ ) as well as on data collected after simulating the pressurized leak ( $t_{end}$ ).

The relative permittivity values retrieved through the hyperbola fitting procedure permitted to restrict the parameter space boundaries of the sand permittivity to small values. The full-wave inversion strategy was subsequently used to refine the values of the parameters retrieved before and after the leak. The relative permittivity values computed for the sand layer ( $\epsilon_{r,1}$ ) and the pipe layer ( $\epsilon_{r,2}$ ) are shown in Fig. 13a whereas the estimates regarding the antenna heights ( $h_0$ ) and pipe depths ( $h_1$ ) are shown in Fig. 13b. As expected, we observe that the antenna height  $h_0$  and the permittivity of the surface sand layer  $\epsilon_{r,1}$  are retrieved with accuracy, either with or without the presence of the leak. The results also highlight that, before the leak, the depth of the pipe retrieved through the optimization procedure is constant (around 0.39 m) and in agreement with the measured value, namely, 38.9 cm. At the final stage of the leak ( $t_{end}$ ),  $h_1$  is constant only for positions ranging from 0.0 m to 0.5 m as well as from 1.1 m to 1.6 m. The values retrieved between 0.5 m and 1.1 m fluctuate between the parameter space bounds considered in the inversions because the data located in this area are part of the field of action of the leak. Resorting to GPR data inversions can therefore be useful to get an idea of the leak extent.

The same conclusions can be drawn for the relative permittivity estimated at the sand-pipe interface ( $\epsilon_{r,2}$ ). The permittivity values oscillate between 3 and 4 and deviates from the permittivity generally assumed for our dry sand (i.e.,  $\epsilon_r = 2.8$ ). It confirms the real impact of the presence of the pipe filled with water even if the impact is not really

substantial in this case. We notice that  $\epsilon_{r,2}$  values estimated between 0 m and 0.5 m are lower after the leak although this area was expected not to be affected by the leak. It is worth noting that this phenomenon is not observed between 1.1 m and 1.6 m. It could be explained by the presence of trapped air in some parts of the pipe which caused constructive and destructive interferences. These interferences led in our case to a larger reflection compared to the sand-water case. Despite this drawback, the results highlight that the quantitative characterization of the materials along the pipe can be useful to bring additional information about the leak.

4.4. 3-D GPR data analysis and visualization

Despite the dynamic nature of leaks, the acquisition of 3-D datasets is essential because it allows discriminating continuous objects such as pipes and cables from stones and other point-like objects, which contributes to restrict the leak search area to targeted zones. It also provides useful information about the buried structures and avoids excavation damages by providing maps containing the positions of the objects buried into the ground.

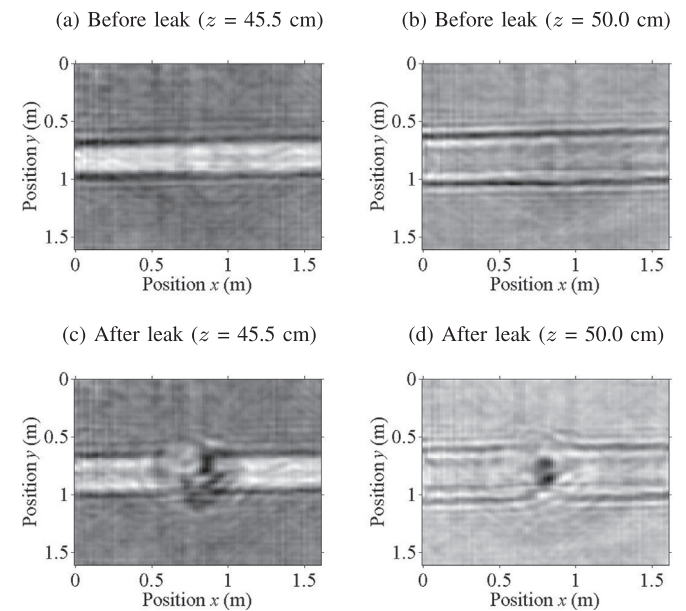


**Fig. 14.** z-slices of the data acquired at (a,c) 45.5 cm and (b,d) 50.0 cm depth at the initial stage ( $t_0$ ) and final stage ( $t_{end}$ ) of the leak, respectively. The data were processed beforehand using the near-field antenna effects removal approach.

A 3-D GPR acquisition permits in particular to create z-slices, i.e., images for which the  $x$  and  $y$  coordinates are projected to a specific depth. Fig. 14 shows the z-slices displayed at 0.455 cm and 0.500 cm depth, respectively, regarding the datasets acquired at the initial stage ( $t_0$ ) and final stage ( $t_{end}$ ) of the leak. The z-slices are showed after having applied the near-field antenna filtering processing step on the 3-D GPR datasets. In absence of leak (Fig. 14a and Fig. 14b), the pipe is easily identified because its reflection is continuous over the successive transects and is well contrasted in comparison to the surrounding medium. These results evidence that the methodology aiming at filtering the antenna effects worked properly for the whole set of transects. At the final stage of the leak (Fig. 14c and d), we observe perturbations that are localized around the central part of the pipe. As especially evidenced in Fig. 14c, the impact of the diffused water on object detection and radar image interpretation can be significant and can cover a quite extended area. The precise localization of the leak position based on Fig. 14c is in fact not straightforward. Conversely, Fig. 14d shows an important and more local reflection located at the position  $x = 0.80$  m and  $y = 0.78$  m in the sandbox. This position corresponds to the path whereby the water was drained by gravity. It is worth mentioning that in more complex media involving several layers having different textures, the determination of the water path would not be so easy. Fig. 14d also evidences that the strong reflections accounting for the pipe (continuity of the hyperbolas) are interrupted close to the leak position. The presence of water out of the pipe leads to wave attenuation and causes destructive interferences, which affects the detection of the hyperbolic reflections. The leak effects are observable above and under the pipe but the importance of the changes noticed in the GPR signal depends on several factors, such as the pressure in the pipe, the texture of the soil surrounding the pipe, the orientation of the leak, etc.

Having a look to different z-slices allows therefore refining the localization of the leak and permits to visualize the importance of the perturbations caused by the leak above and beneath the pipe. From a practical point of view, the end-user generally does not have any information about the initial state of the leak. However, if we assume that the properties of the materials are relatively homogeneous along the pipe, having a look to the pipe several meters away from the leak gives an overview of the pipe reflection without the influence of the leak. In addition to the leak perturbations, the z-slices permit to determine the depth of the pipe, which is an essential aspect required by water supply agencies. The analysis of the 3-D GPR data is therefore a useful tool that brings relevant information about the leak location and the presence of utilities buried into the ground.

Fig. 3a and b show the 3-D datasets acquired at the initial stage ( $t_0$ ) and final stage ( $t_{end}$ ) of the leak, respectively. The data as well as the apexes and pipes identified using the reflection detection and segmentation algorithms are visualized through the new human-computer interface. Before the leak was initiated (Fig. 3a), we observe that the detected apexes are mainly embodied in the form of lines. The two patterns distinguished at the bottom of the image are caused by the PEC and its multiple reflections. The set of points aligned at the center of the 3-D space is located at a depth corresponding to the one at which the pipe is buried. The positions of the apexes are exactly located at the top of the hyperbolas displayed in GPR cross-sections. Nevertheless, it is worth noticing that no apex is detected between the 62<sup>th</sup> and 68<sup>th</sup> transects whereas the hyperbolic-shaped signatures are visible. It therefore prevents the segmentation algorithm to detect the pipe along its total length. In fact, 6 pipe candidates are identified based on the cloud of apexes among which 5 are aligned with the real pipe position. It confirms the ability of the algorithms in finding quite accurately the position of the pipe.

The probability they exist oscillates between 5% and 48%. It is worth noting that the probability actually corresponds to the count of detected apexes that are located along a pipe candidate divided by the total number of points that could potentially be detected along this one. A last pipe candidate is identified at the bottom of the 3-D space whereas it should not be detected. However, the pipe presents a weak existence probability (less than 1%). The results highlights that, even if some improvements are still required to optimize the apex and pipe detection stage, the results have already been satisfying.

After the end of the pressurized leak (Fig. 3b), we observe that the detected apexes are disseminated within the entire 3-D space. Nonetheless, a series of apexes clearly draw a horizontal line split into two parts at the position where the pipe is located. The area which does not really contain apexes in fact corresponds to the position of the leak. The segmentation algorithm detects 7 pipe candidates. All of them are positioned along the axial position of the real pipe. The probability they exist oscillates between 24% and 67% except for one them which presents a lower confidence value (about 5%). It is worth noting that one of the pipe showing a probability value of about 53% begins at the 2<sup>nd</sup> transect and ends at the 75<sup>th</sup> transect. The pipe therefore covers the leak position and makes its detection more difficult to carry out. These results evidence the limitations that are still currently encountered when dealing with the automatic detection of the pipes. However, combining the information provided by the qualitative (GPR image interpretation, automatic detection of utilities, z-slices visualization) and quantitative analyses maximizes the information about the subsurface, and hence, helps detecting leaks in water distribution networks.

## 5. Conclusions and perspectives

In this paper, we proposed a novel and non-destructive integrated tool that takes advantage of advanced radar data processing strategies to help detecting leaks in water distribution networks. The general approach consists in processing GPR data acquired above the area where a leak is suspected. Qualitative data processing strategies are used to improve the interpretation of the 3-D high-resolution subsurface images and to automatically detect underground utilities (stones, cables, pipes ...). The information are then displayed on mobile devices through a specifically designed human-computer interface. Quantitative data analyses are also performed to provide an estimation of the relative permittivity, and hence, the water content, around the distribution pipe. We demonstrated the proof of concept through a laboratory experiment with near-field measurements performed over a leaky pipe buried in a sandbox. The results are very promising and evidence the interest of combining the qualitative information brought by GPR data visualization (structural imagery) with the quantitative information arising from GPR data inversions. Nonetheless, the end-user has to be careful during the interpretation stage because GPR data are influenced by a series of environmental (soil texture, initial volumetric water content ...) and technical (kind and orientation of the leak) factors. Future research will therefore focus on the quantitative reconstruction of heterogeneous media, the integration of the water content information in the end-user interface, the validation of the proof of concept in field conditions and the automatization of the whole processing chain.

## Acknowledgement

This work was supported and funded by the Walloon Region through the "SENSPORT" project (Convention no 1217720) undertaken in the framework of the WBGreen research program. We also benefited from the FNRS-Belgium (Fonds National de la Recherche Scientifique) support and the networking activities carried out within the EU funded COST Action TU1208 "Civil Engineering Applications of Ground Penetrating Radar".

## Appendix A. Description of the main functionalities of the user interface

Functionality	Description
Show Views	Used to manipulate the scene with respect to the required camera. It allows aligning/rotating the view according to the following directions: Front, Back, Top, Bottom, Left and Right.
Show Plan	xy yz xz Used to display or hide images along the XZ plane (cross-sections), the YZ plane (perpendicular images) and/or the XY plane (depth-slices).
Move Image according to Axis	x-Position y-Transsect z -Depth Used to display only one image at a 'Position' x, for a specific 'Transsect' y and/or at a 'Depth' z indicated by the user.
Show Edge	Used to display the edges of the images. The two possible edge detecting methods are <i>Sobel</i> and <i>Frei-Chen</i> . A threshold slider is used to get the most suitable view for each image. Some additional options (not directly available for the user) like invert, gamma, hue, saturation, brightness and others can be used to filter images.
Show Grid	xy yz xz Grid helpers are 2D arrays of lines that take into account the real distance measurements (expressed in meters). The 'Show grid' functionality allows the user to display or hide the grid helper of the XY plane, the YZ plane and/or the XZ plane.
Show Object	Pipe Used to display or hide the pipes detected in the scene. A probability slider can be used to filter out the less probable pipes. Each pipe has a color that represents a probability value. Apex Used to display or hide the apexes detected in the scene. Floor Used to display or hide the map where the survey was conducted from the scene.
Animation	SpeedX SpeedY SpeedZ Stop Used to activate/deactivate the automatic movement of images according to their axis. This option permits the images to move automatically from the first image to the final image and vice-versa with the speed specified by the user. A speed value equal to 0 stops the animation for the corresponding axis. The stop option permits to cancel the animation for all axes.
Setting colors	[0–25%] [25–75%] [75–100%] Used to attribute a specific color to the ranges of index density values. Three ranges are available to express the probability of existence of the pipes.
Save screenshot	Used to save the scene as an image. The user can also save a .text file with comments.
Headtracking	Used to activate/deactivate the detection of the user's face. Face detection allows the user to interact with the application by augmented web gestures. When the option is activated, the user can slightly rotate images by changing the orientation (horizontal and vertical movements) of his head or his device.
Reset	Used to reset the scene to its initial state.
Close controls	Used to allow the user to display or hide the menu of functionalities.

## References

- Ahlberg, C., Shneiderman, B., 1994. Visual information seeking: Tight coupling of dynamic query filters with starfield displays. in Proceedings of the SIGCHI Conference on Human Factors in Computing Systems, Boston, USA, pp. 313–317 Apr.
- Alkhalifeh, K., Craeye, C., Lambot, S., 2014. Design of a 3D UWB linear array of Vivaldi antennas devoted to water leaks detection. Proceedings of the 15th International Conference on Ground Penetrating Radar (GPR 2014), Brussels, Belgium, pp. 783–786 Jul.
- Alkhalifeh, K., Hislop, G., Ozdemir, N., Craeye, C., 2016. Efficient MoM simulation of 3-D antennas in the vicinity of the ground. IEEE Trans. Antennas Propag. 64 (12), 5335–5344 Dec.
- Amran, T., Ismail, M., Ahmad, M., Amin, M., Sani, S., Masenwat, N., Ismail, M., Hamid, S., 2017. Detection of underground water distribution piping system and leakages using ground penetrating radar (GPR). Proceedings of the AIP Conference, vol. 1799, Selangor, Malaysia, pp. 030 004.1–030 004.10 Aug.
- Ardekani, M., Druyts, P., Lambot, S., De Coster, A., Neyt, X., 2014. Recovering the structure of a layered soil, including layer thickness and dielectric permittivity, using the interfaces and objects backscatter detected in gpr b-scans. Proceedings of the 15th International Conference on Ground Penetrating Radar (GPR 2014), Brussels, Belgium, pp. 397–400 Jul.
- Atef, A., Zayed, T., Hawari, A., Khader, M., Moselhi, O., 2016. Multi-tier method using infra-red photography and GPR to detect and locate water leaks. Autom. Constr. 61, 162–170 Jan.
- Ayala-Cabrera, D., Izquierdo, J., Pérez-García, R., Herrera, M., 2011. Location of buried plastic pipes using multi-agent support based on GPR images. J. Appl. Geophys. 75 (4), 679–686 Dec.
- Ayala-Cabrera, D., Herrera, M., Izquierdo, J., Ocaña Levario, S., Pérez-García, R., 2013. GPR-based water leak models in water distribution systems. Sensors 13 (12), 15 912–15 936 Nov.
- Bertolla, L., Porsani, J., Soldovieri, F., Catapano, I., 2014. GPR-4D monitoring a controlled LNAPL spill in a masonry tank at USP, Brazil. J. Appl. Geophys. 103, 237–244 Apr.
- Bimpas, M., Amditis, A., Uzunoglu, N., 2010. Detection of water leaks in supply pipes using continuous wave sensor operating at 2.45 GHz. J. Appl. Geophys. 70 (3), 226–236 Mar.
- Buering, T., Gerken, J., Reiterer, H., 2006. User interaction with scatterplots on small screens - a comparative evaluation of geometric-semantic zoom and fisheye distortion. IEEE Trans. Vis. Comput. Graph. 12 (5), 829–836 Sep.
- Burigat, S., Chittaro, L., 2009. A mobile starfield visualization with space compression capabilities. Proceedings of the 11th International Conference on Human-Computer Interaction with Mobile Devices and Services, Bonn, Germany, pp. 1–2 Sep.
- Calvary, G., Coutaz, J., Thevenin, D., Limbourg, Q., Bouillon, L., Vanderdonck, J., 2003. A unifying reference framework for multi-target user interfaces. Interact. Comput. 15 (3), 289–308 Jun.
- Cataldo, A., Cannazza, G., De Benedetto, E., Giaquinto, N., 2012a. A new method for detecting leaks in underground water pipelines. IEEE Sensors J. 12 (6), 1660–1667 Jun.
- Cataldo, A., Cannazza, G., De Benedetto, E., Giaquinto, N., 2012b. A TDR-based system for the localization of leaks in newly installed, underground pipes made of any material. Meas. Sci. Technol. 23 (10), 1–9 Sep.
- Cataldo, A., Persico, R., Leucci, G., De Benedetto, E., Cannazza, G., Matera, L., De Giorgi, L., 2014. Time domain reflectometry, ground penetrating radar and electrical resistivity tomography: a comparative analysis of alternative approaches for leak detection in underground pipes. NDT & E Int. 62, 14–28 Mar.
- Catapano, I., Affinito, A., Bertolla, L., Porsani, J., Soldovieri, F., 2014. Oil spill monitoring via microwave tomography enhanced GPR surveys. J. Appl. Geophys. 108, 95–103 Sep.
- Charlton, M., Mulligan, M., 2001. Efficient detection of mains water leaks using ground-penetrating radar (GPR). Proceedings of Subsurface and Sensing Technologies and Applications III, vol. 4491, San Diego, USA, pp. 375–386 Jul.
- Cheong, L., 1991. Unaccounted for water and the economics of leak detection. Proceedings of the 18th International Water Supply Congress and Exhibition, Copenhagen, Denmark, pp. 15–31 May.
- Colombo, A., Karney, B., 2002. Energy and costs of leaky pipes: toward comprehensive picture. J. Water Resour. Plan. Manag. 128 (6), 441–450 Nov.
- Crocco, L., Soldovieri, F., Cassidy, N., Prisco, G., 2009. Early-stage leaking pipes GPR monitoring via microwave tomographic inversion. J. Appl. Geophys. 67 (4), 270–277 Apr.
- Crocco, L., Soldovieri, F., Millington, T., Cassidy, N., 2010. Bistatic tomographic GPR imaging for incipient pipeline leakage evaluation. Prog. Electromagn. Res. 101, 307–321.
- Dardenne, X., Craeye, C., 2008. Method of moments simulation of infinitely periodic structures combining metal with connected dielectric objects. IEEE Trans. Antennas Propag. 56 (8), 2372–2380 Aug.
- De Coster, A., Lambot, S., 2017. Full-Wave Removal of Internal Antenna Effects and Antenna-Medium Coupling for Improved Ground-Penetrating Radar. IEEE Transactions on Geoscience and Remote Sensing Accepted.
- Demirci, S., Yigit, E., Eskidemi, I., Ozdemir, C., 2012. Ground penetrating radar imaging of water leaks from buried pipes based on back-projection method. NDT & E International 47, 35–42 Apr.
- Dong, L., Carnalla, S., Shinozuka, M., 2012. GPR survey for pipe leakage detection: experimental and analytical study. SPIE proceedings, Nondestructive Characterization for Composite Materials, Aerospace Engineering, Civil Infrastructure, and Homeland Security, vol. 8347, San Diego, USA, pp. 1–7 Apr.
- Eyuboglu, S., Mahdi, H., Al-shukri, H., 2003. Detection of water leaks using ground penetrating radar. Proceedings of the Third International Conference on Applied Geophysics, Orlando, USA, pp. 1–17 Dec.
- Farley, M., Trow, S., 2003. Losses in water Distribution Networks. IWA Publishing, p. 296 Mar. 1em plus 0.5em minus 0.4em.
- Fuchs, H., Riehle, R., 1991. Ten years of experience with leak detection by acoustic signal analysis. Appl. Acoust. 33 (1), 1–19 Dec.
- Gao, Y., Brennan, M., Joseph, 2009. On the effects of reflections on time delay estimation for leak detection in buried plastic water pipes. J. Sound Vib. 325 (3), 649–663 Aug.
- Geuzaine, C., Remacle, J., 2009. Gmsh: A three-dimensional finite element mesh generator with built-in pre- and post-processing facilities. Int. J. Numer. Methods Eng. 79 (11), 1309–1331 [Online]. Available: <http://gmsh.info>.
- Glaser, D., Werkema, D., Versteeg, R., Henderson, R., Rucker, D., 2012. Temporal GPR imaging of an ethanol release within a laboratory-scaled sand tank. J. Appl. Geophys. 86, 133–145 Nov.
- Halimshah, N., Yusup, A., Amin, Z., Ghazalli, M., 2015. Visual inspection of water leakage from ground penetrating radar radargral. ISPRS Annals of Photogrammetry, Remote Sensing and Spatial Information Sciences, vol. II-2, Kuala Lumpur, Malaysia, pp. 191–198 Oct.
- Hao, T., Rogers, C., Metje, N., Chapman, D., Muggleton, J., Foo, K., Wang, P., Pennock, S., Atkins, P., Swingler, S., Parker, J., Costello, S., Burrow, M., Anspach, J., Armitage, R., Cohn, A., Goddard, K., Lewin, P., Orlando, G., Redfern, M., Royal, A., Sall, A., 2012.

- Condition assessment of the buried utility service infrastructure. *Tunn. Undergr. Space Technol.* 28, 331–344 Mar.
- Hunaidi, O., Chu, W., Wang, A., Guan, W., 2000. Detecting leaks in plastic pipes. *J. Am. Water Works Assoc.* 92 (2), 82–94 Feb.
- Hunaidi, O., Wang, A., Bracken, M., Gambino, T., Fricke, C., 2004. Acoustic methods for locating leaks in municipal water pipe networks. *Proceedings of the International Water Demand Management Conference, Dead Sea, Jordan*, pp. 1–14 May.
- Huyer, W., Neumaier, A., 1999. Global Optimization by Multilevel Coordinate Search. *J. Glob. Optim.* 14 (4), 331–355 Jun.
- Hyun, S., Jo, Y., Oh, H., Kim, S., 2003. An experimental study on a ground-penetrating radar for detecting water-leaks in buried water transfer pipes. *Proceedings of the 6th International Symposium on Antennas, Propagation and EM Theory, Beijing, China*, pp. 596–599 Oct.
- Hyun, S., Oh, H., Jo, Y., Kim, S., Kim, Y., 2007. The laboratory scaled-down model of a ground-penetrating radar for leak detection of water pipes. *Meas. Sci. Technol.* 18 (9), 2791–2799 Jul.
- Kanopoulos, N., Vasanthavada, N., Baker, R., 1988. Design of an image edge detection filter using the sobel operator. *IEEE J. Solidstate Cir.* 23 (2), 358–367 Apr.
- Lagarias, J.C., Reeds, J.A., Wright, M.H., Wright, P.E., 1998. Convergence Properties of the Nelder–Mead Simplex Method in Low Dimensions. *SIAM J. Optim.* 9 (1), 112–147.
- Lai, W., Chang, R., Sham, J., Pang, K., 2016. Perturbation mapping of water leak in buried water pipes via laboratory validation experiments with high-frequency ground penetrating radar (GPR). *Tunn. Undergr. Space Technol.* 52, 157–167 Feb.
- Lambot, S., “Method and device for characterization of physical properties of a target volume by electromagnetic inspection.” US 2014/0019050 A1, Jan. 2014.
- Lambot, S., André, F., 2014. Full-wave modeling of near-field radar data for planar layered media reconstruction. *IEEE Trans. Geosci. Remote Sens.* 52 (5), 2295–2303 May.
- Lambot, S., Slob, E., van den Bosch, I., Stockbroeckx, B., Vanclooster, M., 2004. Modeling of ground-penetrating Radar for accurate characterization of subsurface electric properties. *IEEE Trans. Geosci. Remote Sens.* 42 (11), 2555–2568 Nov.
- Lambot, S., Weiermüller, L., Huisman, J., Vereecken, H., Vanclooster, M., Slob, E., 2006. Analysis of air-launched ground-penetrating radar techniques to measure the soil surface water content. *Water Resour. Res.* 42 (11), W11403 Nov.
- Ledieu, J., De Ridder, P., De Clercq, P., Dautrebande, S., 1986. A method of measuring soil moisture by time domain reflectometry. *J. Hydrol.* 88 (3–4), 319–328 Nov.
- Lee, B., Oh, S., 2017. Modified electrical survey for effective leakage detection at concrete hydraulic facilities. *J. Appl. Geophys.* vol. In Press, Corrected Proof, Aug.
- Liu, Z., Kleiner, Y., 2013. State of the art review of inspection technologies for condition assessment of water pipes. *Measurement* 46 (1), 1–15 Jan.
- Liu, G., Jia, Y., Liu, H., Qiu, H., Qiu, D., Shan, H., 2002. A case study to detect the leakage of underground pressureless cement sewage water pipe using GPR, electrical, and chemical data. *Environ. Sci. Technol.* 36 (5), 1077–1085 Apr.
- Medina, J., Vanderdonck, J., 2016. A tool for multi-surface collaborative sketching. *Proceedings of Third International Workshop on Interacting with Multi-Device ecologies, Niagara Falls, Canada*, pp. 1–8 Nov.
- Nakhkash, M., Mahmood-Zadeh, M., 2004. Water leak detection using ground penetrating radar. *Proceedings of the Tenth International Conference on Ground Penetrating Radar, Delft, The Netherlands*, pp. 525–528 Jun.
- Pal, M., Dixon, N., Flint, J., 2010. Detecting & locating leaks in water distribution polyethylene pipes. *Proceedings of the World Congress on Engineering*, vol. II, London, UK, pp. 1–6 Jun.
- Park, R., 1990. A fourier interpretation of the Frei-Chen edge masks. *Pattern Recogn. Lett.* 11 (9), 631–636 Sep.
- Puust, R., Kapelan, Z., Savic, D., Koppel, T., 2010. A review of methods for leakage management in pipe networks. *Urban Water J.* 7 (1), 22–45 Feb.
- Rizzo, P., 2010. Water and wastewater pipe nondestructive evaluation and health monitoring: a Review. *Adv. Civil Eng.* 2010, 1–13 Feb.
- Rucker, D., Fink, J., Loke, M., 2011. Environmental monitoring of leaks using time-lapsed long electrode electrical resistivity. *J. Appl. Geophys.* 74 (4), 242–254 Aug.
- Sarkis, R., Craeye, C., 2010. Circular array of wideband 3D Vivaldi antennas. *Proceedings of URSI International Symposium on Electromagnetic Theory, Berlin, Germany*, pp. 792–794 Aug.
- Sarkis, R., Craeye, C., Veidt, B., 2011. Thick Vivaldi antenna for focal plane applications. *Proceedings of the IEEE International Symposium on Antennas and Propagation (APSURSI 2011)*, Spokane, USA, pp. 1988–1991 Jul.
- Savić, D., Ferrari, G., 2014. Design and performance of district metering areas in water distribution systems. *Proceedings of the 16th Conference on Water Distribution System Analysis (WDSA)*, vol. 89, Bari, Italy, pp. 1136–1143 Jul.
- Shimanskii, S., Strelkov, B., Ananev, A., Lyubishkin, A., Iijima, T., Mochizuki, H., Kasai, Y., Yokota, K., Kanazawa, J., 2005. Acoustic method of leak detection using high-temperature microphones. *Atomic Energy* 98 (2), 89–96 Feb.
- Skolnik, M., 2008. *Radar Handbook*, Third Edition, ser. Electronics Electrical Engineering, McGraw-Hill Education, p. 1328.
- Soldovieri, F., Crocco, L., Brancaccio, A., Solimene, R., Persico, R., 2011. Applications of ground penetrating radar and microwave tomography in water monitoring and management. *Int. Water Technol. J.* 1 (1), 73–82 Jun.
- Stampolidis, A., Soupios, P., Vallianatos, F., Tsokas, G., 2003. Detection of leaks in buried plastic water distribution pipes in urban places - a case study. *Proceedings of the 2nd International Workshop on Advanced Ground Penetrating Radar, Delft, The Netherlands*, pp. 120–124 May.
- Tang, X., Liu, Y., Zheng, L., Ma, C., Wang, H., 2009. Leak detection of water pipeline using wavelet transform method. *Proceedings of the International Conference on Environmental Science and Information Application Technology, Wuhan, China*, pp. 217–220 Jul.
- Topp, G., Davis, J., Annan, A., 1980. Electromagnetic determination of soil water content: measurements in coaxial transmission lines. *Water Resour. Res.* 16 (3) pp. 574–582–961, Jun.
- Vanderdonck, J., 2005. A mda-compliant environment for developing user interfaces of information systems. In: Pastor, O., Cunha, J.F.E. (Eds.), *Advanced Information Systems Engineering, 17th International Conference, CAISE 2005, Porto, Portugal, June 13–17, 2005, Proceedings, ser. Lecture Notes in Computer Science*, vol. 3520. Springer, pp. 16–31 [Online]. Available: [https://doi.org/10.1007/11431855\\_2](https://doi.org/10.1007/11431855_2).
- Vincent, O., Folorunso, O., 2009. A descriptive algorithm for sobel image edge detection. *Proceedings of Informing Science & IT Education Conference*, 40, pp. 97–107 Macon, United States, Jan.
- Xu, Q., Liu, R., Chen, Q., Li, R., 2014. Review on water leakage control in distribution networks and the associated environmental benefits. *J. Environ. Sci.* 26 (5), 955–961 May.



**A. De Coster** received the M.Sc. degree in agricultural and environmental engineering from the Université catholique de Louvain (UCL), Louvain-la-Neuve, Belgium, in 2012. After working on scientific applied projects, he began a Ph.D. in the Bioscience Engineering Faculty of the same university. He carried out his research within the framework of the SENSPOUR and SEWERMAPPER projects (Walloon Region) and received the Ph.D. degree in Agronomy and Bio-engineering in 2017. He is implied in the EU-funded COST Action TU1208 “Civil Engineering Applications of Ground Penetrating Radar. His research interests include subsurface imaging, hydrogeophysics, electromagnetic modeling for ground-penetrating radar, and inversion for nondestructive characterization of soils and materials. He was part of the Organizing Committee of the 15th International Conference on Ground Penetrating Radar in 2014 and received an Early-Stage Researcher Award in the same conference.



**J.L. Pérez Medina** received his M.S. degree in Computer Science from the Centrocidental Lisandro Alvarado University of Barquisimeto, Venezuela in 2004. He also received a M.S. degree in Information System from the Joseph Fourier University of Grenoble, France in 2006 and a Ph.D. in Computer Science from the same university in 2010. He was Professor at Centrocidental Lisandro Alvarado University between 2002 to 2012 and responsible of a Human Computer Interaction course at the Université catholique de Louvain, Belgium, during the 2015–2016 academic year. He is currently a Senior Researcher at the Université catholique de Louvain, Belgium. Throughout his career he developed a deep knowledge of Computer Science and Human Computer Interaction. Passionate about collaborative design based on models, processes, and cross-surface technologies, he capitalizes on his experience acquired in the academic environments and his strong passion for Modeling Tools and Software Development. His interest in scientific research has been promoted by the desire of facilitating the work of IT managers and models designers by helping them in choosing methods, models and modeling environments adapted to their specific needs.

**M. Nottebaere** received a master in physics from the KULeuven in 2012. Since then he has been working as research engineer for the Royal Military Academy, Belgium. His research interest resides in the exploitation of radar data, both remote sensing data and ground-penetrating data, to retrieve information about the soil surface and the underlying structure and objects



**K. Alkhalifeh** was born in Aleppo, Syria in 1981. He received the Diploma in Electrical and Electronic Engineering, from Aleppo University-Faculty of Electrical and Electronic Engineering, in 2006, and the Master degree in Microwave and Telecommunication from the Université catholique de Louvain (UCL), Belgium, in 2010. From 2011–2017, he worked as a research assistant with the Antenna Research Group, Institute of Information and Communication Technologies, Electronics and Applied Mathematics (ICTEAM), Université catholique de Louvain. On March 2017, he received the Ph. D. degree in applied sciences from the UCL. Since May 2017, he is involved as a Postdoc at the UCL. His research interests include multi-band antenna array design and analysis, Ground Penetrating Radar (GPR) applications, fast numerical methods for electromagnetic fields in finite periodic structures, and near-field imaging.



**X. Neyt** received a master in engineering degree (summa cum laude) from the Université Libre de Bruxelles (ULB) in 1994, a postgraduate degree in Signal Processing (summa cum laude) from the Université de Liège (ULg) in 2004 and a PhD in Applied Science from the Royal Military Academy (RMA) and the Université de Liège in 2008. In 1995 he received the Frerichs Award from the ULB and the special IBM grant from the Belgian National Fund for Scientific Research (NFWO). Since then he has been working as research engineer for the Royal Military Academy, Belgium. In 1996–1997 he was visiting scientist at the French aerospace center (ONERA) and in 1999 at the German aerospace center (DLR). In 1997–1999 he was responsible for the design of the image compression module of the European MSG satellite and in

2000–2007, responsible for the redesign of the ground processing of the scatterometer of the European ERS satellite following its gyroscope anomaly. Since 2008, he is leading the Scatterometer Engineering Support Laboratory for the European Space Agency at the Royal Military Academy. He is now professor at the Communication, Information, Systems and Sensors department of the Royal Military Academy and leading the Radar Signal Processing Research Unit. His research interests are signal processing, radar remote sensing, array processing, bistatic radars and image processing.



**J. Vanderdonckt** (M'04-SM'08) received the M.Sc. Degree in mathematics, the M.Sc. Degree in computer science and the Ph.D Degree from the University of Namur, Belgium, in 1987, 1989 and 1997, respectively. He was Visiting Associate Professor at Stanford University in 2000 and is permanent Invited Professor at Polytechnic University of Valencia. He is currently Full Professor at Louvain School of Management, Université catholique de Louvain, Belgium, where he leads the Louvain Interaction Lab since 1998. His research interests include: human-computer interaction (HCI), engineering interactive computing systems (EICS), intelligent user interfaces (IUI), usability engineering and software engineering. Dr. Vanderdonckt is Associate Editor of ACM Trans. on Interactive Intelligent Systems (TiiS) and Knowledge and Information Systems (KAIS). He is also co-editor-in-chief of the Springer Series of Human-Computer Interaction and the SpringerBriefs in Human-Computer Interaction. He is conference co-chair of IEEE RCIS'2019.



**S. Lambot** (Mxx) received the M.Sc. (magna cum laude) and Ph.D. (summa cum laude) degrees in agricultural and environmental engineering from the Université catholique de Louvain (UCL), Louvain-la-Neuve, Belgium, in 1999 and 2003, respectively. He was with the Delft University of Technology, Delft, The Netherlands, from 2004 to 2005, as a European Marie-Curie Post-Doctoral Scientist. From 2006 to 2012, he was with Forschungszentrum Jülich, Jülich, Germany, as a Research Group Leader. Since 2006, he has been a Professor and FNRS Research Group Leader with UCL. His research interests include electromagnetic modeling for ground-penetrating radar (GPR) and electromagnetic induction, inversion for nondestructive characterization of soils and materials, hydrogeophysics, and remote sensing of

the environment. He has published more than 70 journal papers on these topics. Dr. Lambot was the General Chair of the 3rd International Workshop on Advanced Ground Penetrating Radar in 2005 and General Chair of the 15th International Conference on Ground Penetrating Radar in 2014. He has organized GPR and Hydrogeophysics sessions in the GPR, IWAGPR, AGU, EGU, CMWR, and EAGE international conferences. He was Guest Editor for four Special Issues in Near Surface Geophysics, Vadose Zone Journal and IEEE JSTARS. He was an Associate Editor of Vadose Zone Journal from 2009 to 2014 and he is now Associate Editor for IEEE JSTARS.